Journal of Polymers and the Environment (2024) 32:2192–2206
https://doi.org/10.1007/s10924-023-03127-y

ORIGINAL PAPER

Carboxymethyl Tamarind Xyloglucan-Low Methoxyl Pectinate Stimuli-Responsive IPN Beads Encapsulating an Anti-cancer Drug

Yasir Faraz Abbasi[1] · Hriday Bera[2,1] · Abhimanyu Thakur[3,4]

Accepted: 1 November 2023 / Published online: 18 November 2023
© The Author(s), under exclusive licence to Springer Science+Business Media, LLC, part of Springer Nature 2023

Abstract

To efficiently deliver erlotinib HCl (ERL) to triple-negative breast cancer cells, dual crosslinked interpenetrating polymer network beads composed of carboxymethyl tamarind xyloglucan-grafted poly-*N*-isopropylacrylamide/montmorillonite nanocomposites and low-methoxyl pectin (LMP) were formulated. Incrementing the reinforcing clay in the matrices increased the size of the beads (1.29 ± 0.10 – 1.55 ± 0.28 mm) and improved their drug entrapment efficiency (DEE, 60.62 ± 1.02 – $86.73 \pm 0.25\%$). The results of SEM analyses displayed spherical morphology of the fabricated beads. The compatibility of their constituents with ERL was ensured by infrared, thermal, and X-ray diffraction studies. Moreover, these beads exhibited temperature-sensitive swelling behavior and their molar masses between crosslinks ($\overline{M}_c$), estimated adopting Flory–Rehner equation, were declined with temperature. Various matrices also showed sustained drug release patterns, which were best fitted with the Korsmeyer–Peppas kinetic model and the drug release was driven by Fickian diffusion- mechanism. Furthermore, the beads with the highest MMT content (F-3, 20% MMT) demonstrated pH-sensitive swelling and drug release patterns. These also conferred a faster biodegradability relative to the control scaffolds (F-1, 0% MMT) and enhanced sensitivity on MDA-MB-231 cells as compared to pure ERL. Therefore, CTX/LMP-based IPN beads could be exploited as promising drug-carriers for TNCB therapy.

Keywords Breast cancer therapy · Drug delivery · Tailor-made polysaccharide · Clay particles · Nanocomposites

Introduction

Despite vast exploration of disease etiology and advancements in oncology treatment, cancer remains the major cause of global mortality [1]. This could be partly ascribed to the poor bioavailability, insufficient therapeutic outcomes, and non-specific targeting of various chemotherapeutic agents exploited for cancer treatment [2]. Over several years, polymers have widely been utilized for constructing effective delivery systems of anti-cancer agents with improved therapeutic outcomes [3]. Recently, various polysaccharides have gained an immense interest in developing high-performance carriers of numerous anti-cancer drugs accredited to their excellent biodegradability, biocompatibility and safety profiles [3]. Tamarind xyloglucan (TX) is a neutral, branched polysaccharide obtained from *Tamarindus indica*. It has a cellulose-like backbone comprising xylose, galactoxylose and glucose residues in a molar ratio of 2.25:1.0:2.8 [4, 5]. It has long been employed to fabricate various drug delivery systems owing to its favorable features like excellent drug loading capacity and broad pH tolerance [6]. Carboxymethylation of TX (*i.e.,* CTX) renders anionic character to the polymeric backbone and consequently, enhances its hydrophilicity and drug delivery characteristics [7]. To impart controlled swelling behavior, efficient drug loading capacity and sustained drug release behavior [8], poly (N-isopropyl acrylamide) (PNIPA) could be integrated to the CTX

Yasir Faraz Abbasi and Hriday Bera contributed equally to this work.

✉ Hriday Bera
hriday.bera1@gmail.com

1 Wuya College of Innovation, Shenyang Pharmaceutical University, Shenyang 110013, Liaoning, China

2 Dr. B. C. Roy College of Pharmacy and Allied Health Sciences, Durgapur 713206, India

3 Centre for Regenerative Medicine & Health, Hong Kong Institute of Science and Innovation, CAS Limited, Science Park, Shatin, Hong Kong, China

4 Pritzker School of Molecular Engineering, Ben May Department for Cancer Research, University of Chicago, Chicago, IL, USA

backbone [8]. The grafted PNIPA chains could exhibit a transition from an expanded coil to a tightly entangled structure above its lowest critical solution temperature (LCST, 32 °C), making the scaffolds temperature responsive [4]. Pioneering researchers frequently utilized N,N-methylenebisacrylamide (MBA) to copolymerize PNIPA chains, which support the structure of well-extended PNIPA networks and improve their hydrophilicity and pH sensitivity [9]. The cross-linking of PNIPA hydrogels in the presence of smectite clay particles like montmorillonite (MMT) could further increase the mechanical, thermal and swelling characteristics of the polymeric matrixes. MMT is a 2:1 layered silicate and could effectively interact with PNIPA chains, affording organoclay nanocomposites (NCs) [10]. The intercalated or exfoliated MMT within the NCs could entrap various drug molecules and eventually augment their solubility and stability in the physiological environment. Moreover, MMT improves the dissolution and bioavailability of hydrophobic drugs [11, 12].

Now-a-days, several researchers have fabricated TX-based interpenetrating polymer network (IPN) matrices by incorporating another polysaccharide template for the sustained delivery of drugs [13–15]. Pectin has been a special-interest polysaccharide for the last few decades owing to its health benefits and drug delivery attributes. Its main chain primarily comprises of α-(1, 4)-D-galacturonic acid residues with different percentages of esterified carboxyl units [16]. Based on the degree of esterification (DE), pectin is classified into low-methoxyl pectin (LMP, DE < 50%) and high-methoxyl pectin (HMP, DE > 50%) [16]. Compared to the requirements of plenteous sugar and concentrated acidic medium for constructing HMP-based gels, LMP could form ionically crosslinked rigid hydrogel beads with divalent metal cations, under a mild acidic condition (pH range, 2.0 to 6.0) without sugar [16]. The IPN structures of LMP with other polysaccharides are commonly afforded by simultaneous ionotropic gelation and covalent crosslinking protocols. Thus, CTX-*g*-PNIPA/MMT NC entangled LMP-based IPN beads could be accomplished by crosslinking with ionic (viz., Zn^{+2}) and covalent (*i.e.,* glutaraldehyde, GA) crosslinkers and the resulting matrices could effectively be employed for the oral controlled delivery of erlotinib HCl (ERL).

ERL is a tyrosine kinase (TK) inhibitor (TKI), which interferes epidermal growth factor receptor (EGFR) autophosphorylation and interrupts TK-mediated pathways associated to proliferation, invasion and metastasis of human tumor cells [17]. ERL is currently overprescribed in treating triple-negative breast cancer (TNBC), accredited to the strong association of EGFR with TNBC [18]. Although numerous particulate systems have been engineered for oral controlled delivery of ERL in TNBC, to the best of our knowledge, thermo/pH-responsive CTX-*g*-PNIPA/MMT NC blended LMP-based IPN beads as ERL carriers have not yet been reported in the literature. To fill the research gaps, it was hypothesized that the CTX/LMP based IPN beads would display thermo/pH sensitivity and efficiently deliver ERL to improve its sensitivity in TNBC cells. To test these hypotheses, the primary aims of our present study were to afford different ERL-loaded CTX-*g*-PNIPA/MMT NC-reinforced LMP-based IPN beads and structurally characterize them employing various analytical tools. Subsequently, their drug release, thermo/pH responsive swelling and biodegradable behaviors were evaluated. Lastly, the potentials of carriers to increase the sensitivity of ERL on TNBC cells were assessed systemically.

Materials and Methods

Materials

ERL (Laurus Labs Ltd., India) and TX (Mw, 6.97 × 105 g/mol; moisture content, 10%, pH, 6.00–8.00, Maruti Hydrocolloids, India), GENU® pectin LM-104 AS-FS (Mw, ~ 30,000 g/mol, degree of esterification, 28% and degree of amidation, 20%, CPKelco, Denmark) were received as gift samples. MMT was purchased from Qualigens Fine Chemicals, India. NIPA, MBA, tetramethylethylenediamine (TMED), potassium persulfate (KPS), proteinase K, and lysozyme were procured from Sigma Aldrich, USA. For cell studies, human MDA-MB-231 cells (NCCS, India), MTT reagent (Sigma Aldrich, USA), fetal bovine serum (FBS, Invitrogen, USA), cell culture medium (Invitrogen, USA), Alexa Fluor® 488 conjugated anti-rabbit secondary antibody (Cat# A11034, Thermo Fisher Scientific, USA), anti-Annexin primary antibody (Cat# ab14196, Abcam, USA), and VECTASHIELD® containing DAPI (Vector labs, USA) were used.

Synthesis and Characterization of CTX-*g*-PNIPA/MMT NCs

Initially, native TX was carboxymethylated to produce CTX based on our previous study [19]. Subsequently, the CTX-*g*-PNIPA/MMT NCs (NC-1–NC-3) were synthesized as per the earlier reported protocol [19]. Briefly, an aqueous KPS solution (0.1 g/2 ml) was introduced in a three-necked round bottom flask containing an aqueous dispersion of CTX (1 g/20 mL). The mixture was stirred continuously for 10 min under constant nitrogen purging at 40 °C. Subsequently, a dispersion consisting TEMED (10 µl), MBA (0.05 g), NIPA (5 g), and MMT (0/10/20% w/w of NIPA) was introduced and allowed for polymerization reactions at 70 °C for 3 h. The obtained NCs were then quenched using copious deionized water, washed with excess 80% v/v

methanol, filtered and dried at 55 °C to constant weights. Their grafting (%) was calculated using the following equation:

$$\text{Grafting } (\%) = \frac{W_2 - W_1}{W_1} \times 100 \quad (1)$$

The W_2 and W_1 denote the weights of grafted polymers and CTX, respectively. The ^{1}H NMR spectra of pure TX, CTX, NIPA, NC-1 and NC-2 were obtained on NMR spectrometer (Bruker DPX-300, country) at 300 MHz using DMSO-*d*6 as solvent. Different samples were also scanned under scanning electron microscopy (SEM, JSM6360A, JOEL, Japan) to examine their morphological appearances at an accelerating voltage of 20 kV.

Formulation of ERL-Loaded CTX/LMP-Based IPN Beads

The resulting NCs (NC-1–NC-3) were utilized to formulate ERL-loaded CTX/LMP-based IPN beads (viz., F-1–F-3, respectively) following simultaneous ionotropic gelation and covalent crosslinking techniques as reported elsewhere [19]. Concisely, accurately weighed quantities of NCs (250 mg) were soaked overnight in distilled water. Afterward, LMP (750 mg) and ERL (100 mg) were added to it and the mixtures were magnetically stirred for 6 h. Following homogenization at 5000 RPM for 20 min, the dispersions were extruded through 21G needles into a mildly agitated zinc acetate (5% w/v) solution containing GA (2.5% v/v). The beads thus formed (F-1–F-3) were allowed to remain in the crosslinking solution for 30 min, collected by filtration and repeatedly washed with plenty of distilled water to completely eliminate unreacted GA. This was confirmed by the negative test of the washings with Brady's qualitative reagent (2,4-dinitrophenylhydrazine). The beads were then dried at room temperature for 24 h and stored in a desiccator.

Beads Size, Shape and Porosity

The average diameter of 100 beads was determined using digital slide calipers (CD-6 CS, Mitutoyo Corporation, Japan). The scanning electron microscopy (SEM, JSM6360A, JOEL, Tokyo, Japan) was also exploited to examine the surface morphologies of the drug-loaded beads (F-1 and F-3).

The porosity of beads (F-1 and F-3) was evaluated by the liquid displacement method using ethanol as the displacement liquid [20]. The beads of known weight (W_i) were emerged in ethanol and soaked for 24 h to allow ethanol to penetrate into their pores. The final weight of the beads (W_f) was recorded and their porosity (%) was calculated according to the following equation:

$$Porosity(\%) = \frac{W_f - W_i}{\rho_{ethanol} \times V} \times 100 \quad (2)$$

the $\rho_{ethanol}$ and V refer to the density of ethanol and volume of beads, respectively.

Drug Entrapment Efficiency (DEE) and Drug Loading (DL)

The extent of drug entrapment and loading within the beads was determined by dispersing an accurately weighed (100 mg) and crushed beads into 500 ml of 0.1 N HCl (pH 1.2). The volumetric flask containing the dispersion of beads was then continuously agitated at 120 RPM for 24 h at room temperature. Later, it was passed through a membrane filter (diameter, 0.2 µm). Finally, the drug content in the filtrate was assayed spectrophotometrically (Shimadzu/UV-1700, Japan) at 342 nm. The DEE and DL values were then determined based on the following relationships:

$$DEE(\%) = \frac{M_{actual}}{M_{theoeritcal}} \times 100 \quad (3)$$

$$DL(\%) = \frac{M_{actual}}{M_{beads}} \times 100 \quad (4)$$

the M_{actual} is the assayed ERL content in the given weight of the beads (M_{beads}) and $M_{theoretical}$ represents the theoretical quantity of ERL added during the preparation of beads.

Solid State Characterization of ERL-Loaded Beads

The FT-IR analyses of pure ERL, F-1 and F-3 were performed by scanning them under Perkin Elmer 1600 FT-IR Spectrometer (Perkin Elmer, USA) within a wavenumber range of 4000 to 500 cm^{-1}. In addition, DSC thermograms of samples were recorded on a differential scanning calorimeter (Pyris 1, Perklin Elmer, USA) at a constant heating rate of 10 °C min^{-1} over a broad temperature range (50–300 °C). The thermal properties of ERL, F-1 and F-3 were further examined using a thermogravimetric analyzer (STARe SW 10.00, Mettler-Toledo, USA) at a maintained heating rate of 10 °C min^{-1} over a temperature range of 30–300 °C. Moreover, these specimens were analyzed under CuKα radiation detector-coupled powder X-ray diffractometer (P-XRD, Bruker-AXS D8, Germany). The XRD scanning of various samples was carried out from 10 to 50° (2θ) at an anode voltage of 40 kV and input current of 30 mA.

Drug Release

Drug release studies of ERL-loaded IPN beads (F-1–F-3) were conducted in acidic media (0.1 N HCl, pH 1.2) for an

initial 2 h and then continued in phosphate buffer (pH 6.8) for another 6 h in a USP Type II apparatus (Electrolab dissolution tester, TDT-08, India) with paddle rotation speed of 50 rpm at 37 ± 0.5 °C. The aliquots were withdrawn at predetermined time intervals and analyzed by UV–vis spectrophotometer (Shimadzu/UV-1700, Japan).

To examine the pH-dependent drug release profiles of the selected beads (F-3), the experiments were also separately carried out in 0.1 N HCl (pH 1.2) and phosphate buffer (pH 6.8) for 8 h.

Drug Release Data Treatment

The drug release data were fitted in various mathematical kinetic models such as zero-order ($Q = k_0 t + Q_0$), first-order ($Q = Q_0 e^{kt}$), Higuchi ($Q = k_H t^{1/2}$), Hixson–Crowell ($Q^{1/3} = k_{HC} t + Q_0^{1/3}$) and Korsmeyer–Peppas ($Q/Q_\infty = k_{KP} t^n$) models [21]. Based on the n values estimated from the Korsmeyer-Peppas model, the drug release mechanisms of different formulations were determined. Variable n values suggested different drug release mechanisms like Fickian diffusion (n = 0.43), non-Fickian diffusion (n = 0.85), anomalous transport (0.43 < n < 0.85) and super Case II model (n > 0.85). [22]. Furthermore, dissolution efficiency (DE) and mean dissolution time (MDT) of different IPN beads were calculated using the following equations [21]:

$$DE = \frac{\int_0^t y \times dt}{y_{100}} \times 100 \tag{5}$$

$$MDT = \frac{\sum_{j=1}^{n} \hat{t}_j \times \Delta M_j}{\sum_{j=1}^{n} \Delta M_j} \tag{6}$$

the y represents the amount of drug released, j is the sample number, $\hat{t}$ indicates the midpoint time between t_j and t_{j-1}, and ΔM_j refers to the additional amount of drug dissolved between t_j and t_{j-1}.

The initial diffusion coefficients (D_I), average diffusion coefficient (D_A) and late diffusion coefficients (D_L) of different IPN beads were then estimated according to following relationships [23].

$$M_t/M_\infty = 4\left(D_I t/\pi l^2\right)^{0.5} \tag{7}$$

$$DA = 0.049 l^2/t^{\frac{1}{2}} \tag{8}$$

$$M_t/M_a = 1 - \left(8/\pi^2\right) \exp\left[-\pi^2 D_L t/l^2\right] \tag{9}$$

the M_t and M_∞ represent the amount of drug released at time t and at equilibrium, respectively, l denotes the thickness of the beads and $t_{1/2}$ implies the time required for 50% drug release.

Swelling Behavior

To assess the temperature-sensitivity of different ERL-loaded beads, the samples were incubated in distilled water for 24 h at variable temperatures (4, 22 and 45 °C) and their equilibrium swelling (%) was estimated utilizing the following equation [24]:

$$Swelling(\%) = {W_t - W_0}/{W_0} \times 100 \tag{10}$$

the W_0 and W_t represent the initial and final weights of the beads, respectively.

Based on the swelling (%) of IPN beads, their structural parameters such as molecular weights of the polymer chains between two neighboring crosslinks ($\overline{M}_c$), volume fractions in the swollen state (ϕ), Flory–Huggins interaction parameter (χ) and crosslink density (ρ) were determined following Flory–Rehner equations [21, 25].

$$\overline{M}_c = -\rho_s V_s \Phi^{1/3} \left[\ln(1-\Phi) + \Phi + \chi\Phi^2\right]^{-1} \tag{11}$$

$$\Phi = \left[1 + \frac{\rho_s}{\rho_p}\left(\frac{W_a}{W_b}\right) - \frac{\rho_s}{\rho_p}\right]^{-1} \tag{12}$$

$$\chi = \left[\Phi(1-\Phi)^{-1} + N\ln(1-\Phi) + N\Phi\right] \times \left[2\Phi - \Phi^2 N - \Phi^2 T^{-1}(d\Phi/dT)^{-1}\right]^{-1} \tag{13}$$

$$\chi = \left[\Phi(1-\Phi)^{-1} + N\ln(1-\Phi) + N\Phi\right] \times \left[2\Phi - \Phi^2 N - \Phi^2 T^{-1}(d\Phi/dT)^{-1}\right]^{-1} \tag{14}$$

in the above equations, ρ_p and ρ_s are the densities of polymer and solvent, respectively, while V_s designates the molar volume of swelling agent. The W_a and W_b are the weights of polymers after and before swelling, respectively. $N = \left(\frac{\Phi^{2/3}}{3} - \frac{2}{3}\right)\left(\Phi^{1/3} - \frac{2\Phi}{3}\right)^{-1}$, and $d\Phi/dT$ is the slope obtained by plotting the volume fraction data versus temperature.

The swelling profiles of selected IPN beads (F-3) was also evaluated separately in the acidic (0.1 N HCl, pH 1.2) and neutral (phosphate buffer; pH 6.8) media at 37 ºC for 8 h and compared. The water penetration velocity into the beads was also evaluated using the following formula:

$$V = {}^{1}/_{2\rho A} \times {}^{d_w}/_{d_t} \quad (15)$$

the d_w/d_t refers to the slope of swelling (%) versus time curve, ρ represents the density of fluid at 310 K, and A is the surface area of beads, which was calculated based on their average radius (r):

$$A = 4\pi r^2 \quad (16)$$

the average radius of about 100 beads was determined using Vernier caliper.

Biodegradability

The biodegradability of F-1 and F-3 was determined following an earlier published report [26]. Briefly, accurately weighted beads (100–150 mg) were separately dispersed in lysozyme (5×10^4 U/ml) and proteinase K (10 µg/ml) in phosphate-buffered saline (PBS). The dispersions were incubated at 37 °C for 3 h to achieve equilibrium swelling. After removing surface water, the swollen beads were weighted (W_0), subsequently immersed in fresh enzymatic solutions and incubated at 37 °C. The samples were withdrawn at scheduled time points and weighted (W_1) after washing with distilled water and blotting. The gradual weight loss with time was determined in terms of % degradation based on the following expression:

$$Degradation(\%) = {}^{W_0 - W_1}/_{W_0} \times 100 \quad (17)$$

Cell Culture Experiments

Cell viability Assay

The cells viability was evaluated by employing MTT assay protocol, as reported previously [27]. In brief, the MDA-MB-231 cells (5×10^3 cells/well) were seeded in the 96-well plates. The cells were then separately treated with vehicle (*i.e.,* control), placebo F-3, ERL and drug-loaded F-3 for 24 h. The MTT reagent (10 µl of stock concentration of 12 mM) was then introduced into each well. In continuation, the plates were incubated for the next 4 h followed by the removal of contents from each well and subsequent addition of DMSO (150 µl). The absorbance of the plates was subsequently measured on a microplate reader (BioTek Synergy™ H1, Agilent Technologies, USA) at 570 nm and cell viability was calculated using the following expression:

$$\%Cellviability = {}^{A_{sample}}/_{A_{control}} \quad (18)$$

the A_{sample} represents the absorbance of contents of the wells treated with ERL, placebo F-3 and drug-loaded F-3 and $A_{control}$ corresponds to the absorbance of the contents of the wells treated with vehicle. The images of the cells were also captured prior to adding MTT reagent to examine their morphological changes.

Apoptosis

The immunocytochemistry protocol was adopted to identify apoptotic potentials of ERL and drug loaded beads (F-3) on MDA-MB-231 cells [28]. Briefly, when 60 – 70% confluence was achieved, the cells were seeded on 12 mm cover glasses placed in each well of the 24-well plates and treated with vehicle control, ERL and F-3 for 48 h. After washing with 1 × PBS for 5 times, the cells were fixed with 4% paraformaldehyde (PFA) and permeabilized with 0.1% Triton X-100. The blocking of cells was then carried out with 2% bovine serum albumin (BSA) for 1 h at room temperature followed by overnight incubation at 4 °C in a solution comprising anti-Annexin primary antibody (ratio = 1:200). The cells were subsequently washed with PBST (PBS containing 0.1% Tween-20) and incubated in Alexa Fluor® 488 conjugated anti-rabbit secondary antibody. Finally, the cells were stained with Vectashield containing DAPI and observed under a confocal microscope (Zeiss LSM 880 Confocal Microscope, USA).

Statistical Analyses

The numerical data of various experiments were analyzed by one-way ANOVA or unpaired *t*-test and were presented as mean ± standard deviation. The *p*-values lower than 0.05 were typically adopted as statistically significant.

Results and Discussion

Synthesis and Characterization of CTX-*g*-PNIPA/MMT NCs

The carboxymethyl TX (*i.e.,* CTX) was initially afforded by Williamson ether synthesis protocol [29]. The hydroxyl moieties of the TX backbone interacted with NaOH to produce TX alkoxide, which further reacted with monochloroacetic acid to accomplish CTX. The degree of substitution estimated based on acid–base titration method was found to be 0.53 (Fig. 1). Subsequently, CTX-*g*-PNIPA/MMT NCs was synthesized employing a free radical polymerization protocol (Fig. 1) [21]. The decomposition of KPS in the presence of KPS/TEMED redox system under a nitrogen atmosphere could generate persulphate radicals, which abstracted hydrogen atoms from the hydroxyl groups of CTX

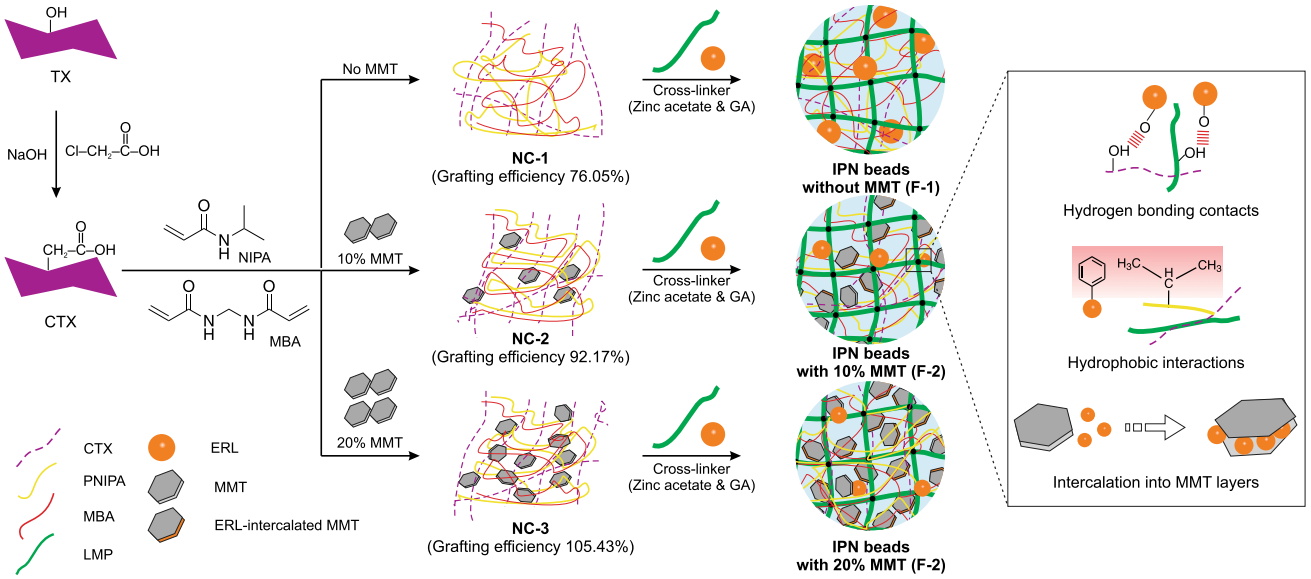

Fig. 1 Synthesis of CTX-*g*-PNIPA/MMT NCs and formulation of ERL-loaded CTX/LMP based IPN beads illustrating possible interactions between drug and polymeric matrices

Table 1 Composition of CTX/LMP based IPN beads and their yields, average diameters, DL and DEE values

Formulation code	Composition[a]					Yield (%)[b]	Diameter (mm)[b]	DL (%)[b]	DEE (%)[b]
	NC type	Grafting efficiency (%)	NC (mg)	LM-pectin (mg)	ERL (mg)				
F-1	NC-1	76.05	250	750	100	96.54 ± 2.50	1.29 ± 0.10	5.51 ± 0.09	60.62 ± 1.02
F-2	NC-2	92.17	250	750	100	97.12 ± 3.62	1.51 ± 0.11	6.69 ± 0.14	74.67 ± 1.52
F-3	NC-3	105.43	250	750	100	96.85 ± 3.82	1.55 ± 0.28	7.88 ± 0.02	86.73 ± 0.25

[a]Crosslinked with 5% zinc acetate and 2.5% glutaraldehyde

[b]Mean ± S.D, n = 3

chains, leading to the graft polymerization of NIPA monomers onto the polysaccharide backbone. The crosslinked interchain bridges were also formed through the covalent attachment of MBA molecules during the polymeric chain propagation. The copolymer chains further anchored to the MMT particles and produced NC architectures (Table 1). The grafting percentage of various NCs was raised with increasing MMT concentrations. This was ascribed to the enhanced accessibility of the monomers to the macroradical sites of the polysaccharide chains in the presence of MMT molecules [23]. The NCs afforded crosslinked structures via. recombination-based termination reactions.

The ^{1}H NMR spectra of TX, CTX, NIPA, NC-1, and NC-2 are presented in Fig. 2A. The ^{1}H NMR spectrum of native TX exhibited characteristic peaks of sugar ring protons and anomeric protons in a narrow region between δ 3.0 and 4.0 ppm. In the spectrum of CTX, the peak at δ 2.2 was attributed to carboxymethyl groups. The NIPA displayed peaks at δ 1.1, 3.4, 3.9 and 5.6–8.0 ppm in its ^{1}H NMR spectrum, which were accredited to its CH_3, CH_2, CH, and $CONH_2$ protons, respectively. Several signals of NIPA were emerged in the spectra of NC-1 and NC-3, confirming the grafting of PNIPA chains on the polysaccharide backbone [30].

SEM images further demonstrated the morphological changes of TX following its carboxymethylation (Fig. 2B). For instance, the TX illustrated granular surfaces, while the CTX exhibited smooth meadow-like structure with few ridges and minor cracks. Following graft copolymerization with PNIPA chains, morphological characteristics of CTX were drastically altered. The NCs revealed rough and slightly protuberant surfaces. The NC-1 manifested a remarkably amplified interlacing system with anomalous pores on their surfaces. This could be credited to the robust coulombic repulsions among CTX carboxylate anions (−COO^{-}) during polymerization [31]. In NC-3, the MMT molecules might reduce the interacting forces among the polymer chains,

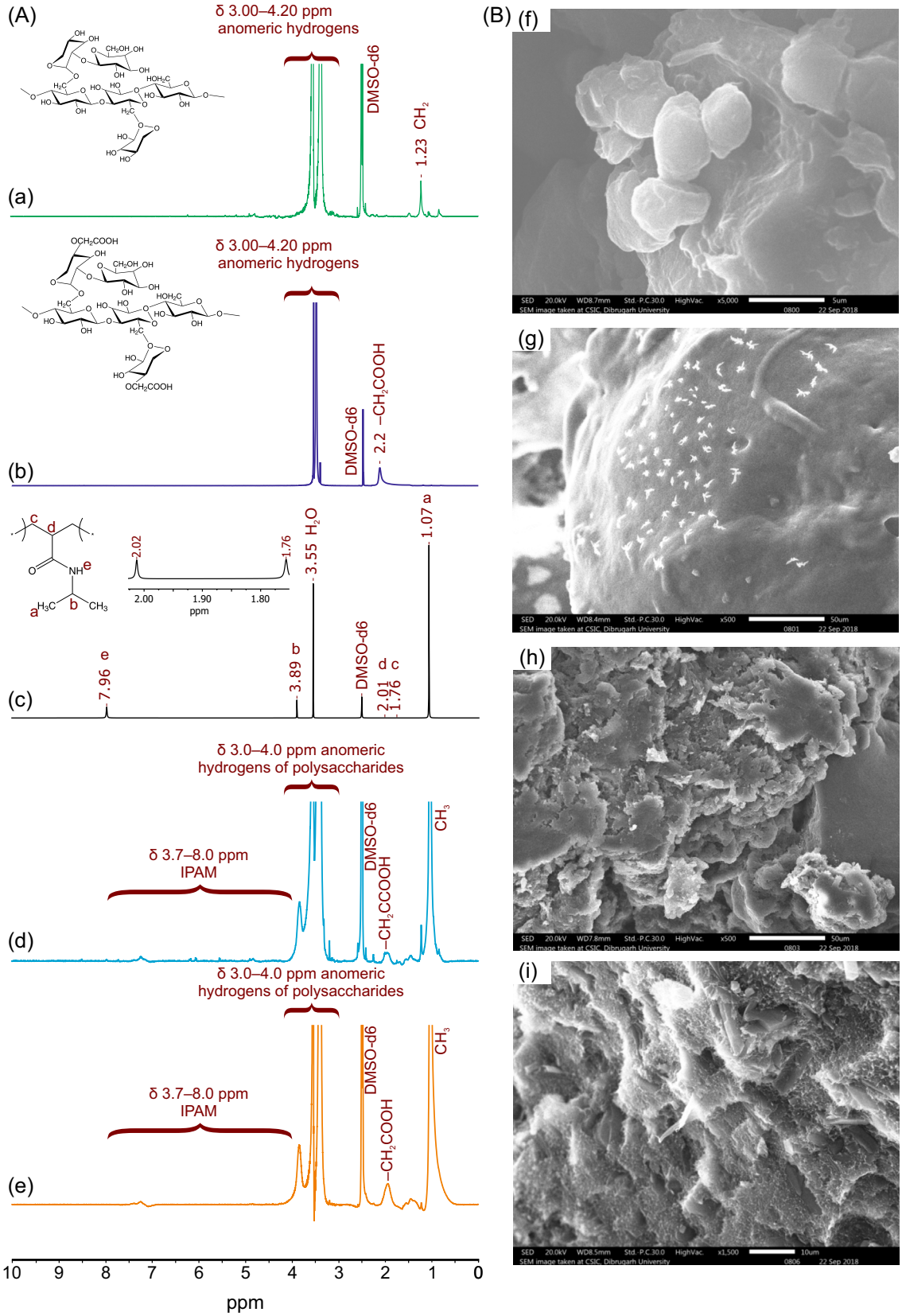

Fig. 2 1HNMR (**A**) of pure TX (a), CTX (b), NIPA (c) and NC-1 (d) and NC-3 (e) and SEM images (**B**) of TX (f), CTX (g), NC-1 (h) and NC-3 (i)

which culminated in the construction of rigid surfaces with reduced porosity [23].

Formulation of CTX/LMP-Based IPN Beads

The CTX-*g*-PNIPA/MMT NC reinforced LMP-based IPN beads entrapping ERL were formulated through a combination of ionic gelation and covalent crosslinking techniques (Fig. 1 and Fig. S1). When the homogenous aqueous dispersion of ERL, LMP and NCs was introduced drop-wise into the gelling bath consisting GA (2.5% w/v) and zinc acetate (5% w/v), the simultaneous covalent and ionic crosslinking of the CMTG/LMP blends could form IPN matrices with high yield (> 96%) (Table 1) and spontaneously entrapped ERL molecules. The concentrations of crosslinking solution could influence the size, morphology, drug entrapment efficiency and release profiles of beads. In the current research, the selected concentrations of crosslinkers, which were chosen based on the previous literature [32, 33], could effectively produce rigid matrices with acceptable physicochemical properties. The electrostatic interactions between the Zn^{+2} ions and carboxylic (COO^{-}) groups of LMP could result in the creation of an "Egg-Box" model structure [23]. Consequently, the fluidity of CTX/MMT NCs was greatly restricted in the crosslinked LMP gels, leading to an enhanced conglomeration. Moreover, the Van der Waals forces and hydrogen bonding contacts between LMP and CTX chains might be crucial in hydrogel bead production. The aldehyde (CHO) moieties of GA also interacted with the OH groups of polysaccharides and formed acetal linkages. In addition, MMT could elicit additional co-crosslinking points to afford rigid matrices [34]. The ERL molecules could establish different non-covalent interactions such as hydrophobic interactions and hydrogen bonding contacts with the polymeric matrices (Fig. 1) [35].

Beads Size, Morphology and Porosity

The average size of ERL-loaded beads ranged from 1.29 ± 0.10 to 1.55 ± 0.28 mm (Table 1). A greater extent of crosslinking in the presence of zinc acetate and GA caused an amplified level of matrix shrinkage and the production of compact composites with smaller particle diameters [23]. Increasing MMT contents enhanced the bead diameter (Table 1). The presence of MMT could increase the viscosity of the polymeric dispersions, which might in turn impede the easy breaking up of droplets into smaller particles [23]. Moreover, the MMT molecules could interrupt the reticulation process of α-L-guluronic acid residues of LMP, affording larger composite particles (F-2 and F-3) [36].

The SEM images displayed a roughly spherical shape with fissures and wrinkles throughout the surfaces of ERL-loaded beads (Fig. 3A). The clay-free beads (F-1) demonstrated irregular morphology. In contrast, MMT-reinforced composite beads (F-3) exhibited regular and rigid surfaces, possibly on account of the strong interfacial interactions among polysaccharide molecules and clay particles [36]. The SEM micrographs captured at higher magnification also conferred several tiny pores and channels over the exterior surfaces of the matrices. These could be formed during the drying process of the beads because of the evaporating water molecules. The size of the pores of MMT-free beads (F-1) was relatively larger than that of clay-reinforced matrices (F-3) [Fig. S2]. The drying process could also distinctively constrict several structural constituents, eventually resulting in slight distortion of the shapes of the beads [23].

The porosity (%) of the beads was determined based on liquid displacement method [20]. The outcomes of the study indicated that the porosity (%) of beads was declined with increasing their clay content [Fig. S3]. These were consistent with the results of SEM image analyses.

Drug Contents

The ERL-entrapped beads demonstrated high drug entrapment efficiency (DEE, 60.62 ± 1.02 – 86.73 ± 0.25%) with DL values ranging from 5.51 ± 0.09 to 7.88 ± 0.02 (Table 1). The strong hydrophobic and hydrogen bonding interactions between LMP and CTX-*g*-PNIPA/MMT NCs before crosslinking could act as a barrier to restrict the outflow of ERL. Additionally, the concomitant covalent and ionic crosslinked biopolymers produced stiffer composite matrices and consequently retained the entrapped ERL molecules by limiting their diffusion into the external media. Thus, the resulting beads exhibited higher DEE [37]. The layered silicate structure of MMT augmented the surface area of polymeric matrices [38] and consequently, the drug entrapment was significantly enhanced ($p < 0.05$) with increasing MMT contents in the beads. Additionally, a greater bead diameter of F-3 could accommodate a higher amount of ERL with improved DEE values.

Solid State Characterization

The fabricated beads were characterized by FTIR, DSC, TGA and PXRD analyses (Fig. 3B–E). The FTIR spectra of ERL displayed various characteristics peaks at 3277 cm^{-1}, 1628 cm^{-1}, 1506 cm^{-1} and 891 cm^{-1} for N–H stretching, N–H bending, C=C stretching and aliphatic ether stretching, respectively (Fig. 3B) [39]. The distinct signals of ERL in the FT-IR spectra of IPN beads (F-1 and F-3) indicated the successful fabrication of drug-loaded beads without any chemical incompatibilities between drug and matrix constituents. However, a minor drifting of various absorption bands of ERL in the IR spectra of drug-loaded beads might

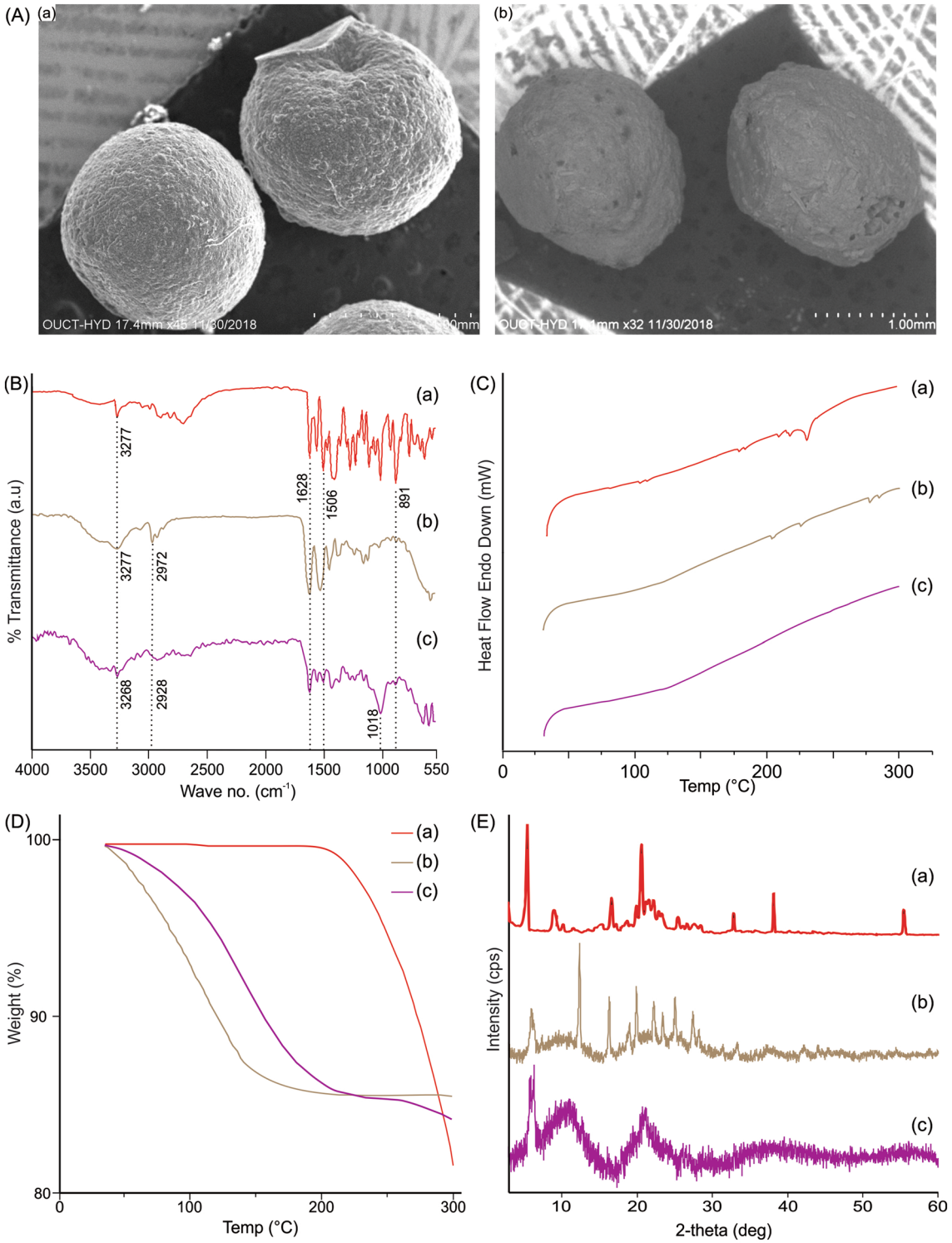

Fig. 3 SEM images (**A**) of ERL-loaded IPN beads [F-1 (a) and F-3 (b)]. FT-IR (**B**), DSC (**C**), TGA (**D**), and P-XRD (**E**) curves of pure ERL (a), ERL-loaded IPN beads with 0% MMT (F-1) (b) and 20 % MMT (F-3) (c)

be attributed to the physical interactions between drug molecules and matrix components, such as hydrogen bonding contacts and dipole–dipole interactions [36].

DSC thermogram of ERL displayed a clear and intense melting peak at 224 °C ascribed to its crystalline and anhydrous structure (Fig. 3C) [39]. In contrast, a thermal event

within 30–100 °C was evidenced in the DSC patterns of ERL-loaded formulations (F-1 and F-3), implying the evaporation of their physisorbed water molecules. Moreover, the molecular dispersion of the drug into the composite matrices partially vanished melting endothermic peaks of ERL in the DSC graphs of ERL-loaded beads (F-1 and F-3) [23].

The thermal decomposition of pure ERL was started above 200 °C (Fig. 3D) [40]. On the other hand, the temperature-induced mass loss of ERL-loaded beads (F-1 and F-3) was drastically enhanced as compared to native ERL. This could be ascribed to the possible transition of crystalline ERL molecules to their amorphous states in the composites, eventually increasing the thermal decomposition rates of ERL-loaded beads (F-1 and F-3) within the experimental temperature range [21]. The clay-free brads (F-1) demonstrated a higher weight loss in comparison to MMT-reinforced matrices (F-3), possibly because of the thermal insulation effects of the MMT molecules [23].

The *P*-XRD patterns of ERL and ERL-loaded beads are illustrated in Fig. 3E. In the *P*-XRD diffractograms of pure ERL, well-resolved and intense peaks were observed, which denoted its crystalline characteristics [39]. However, diffraction patterns of MMT-free matrices (F-1) portrayed a significant fading or complete disappearance of various XRD signals of ERL molecules. This could be accredited to the dispersion of ERL molecules within the matrices, forming a solid solution phase in the polymeric network. A further decline in the intensity of ERL's XRD signals in the presence of MMT (F-3) suggested a more complete transformation of ERL molecules from their crystalline states to amorphous phases [21].

Drug Release

The drug dissolution rates of various IPN matrices were faster as compared to pure ERL (Fig. 4A), which could

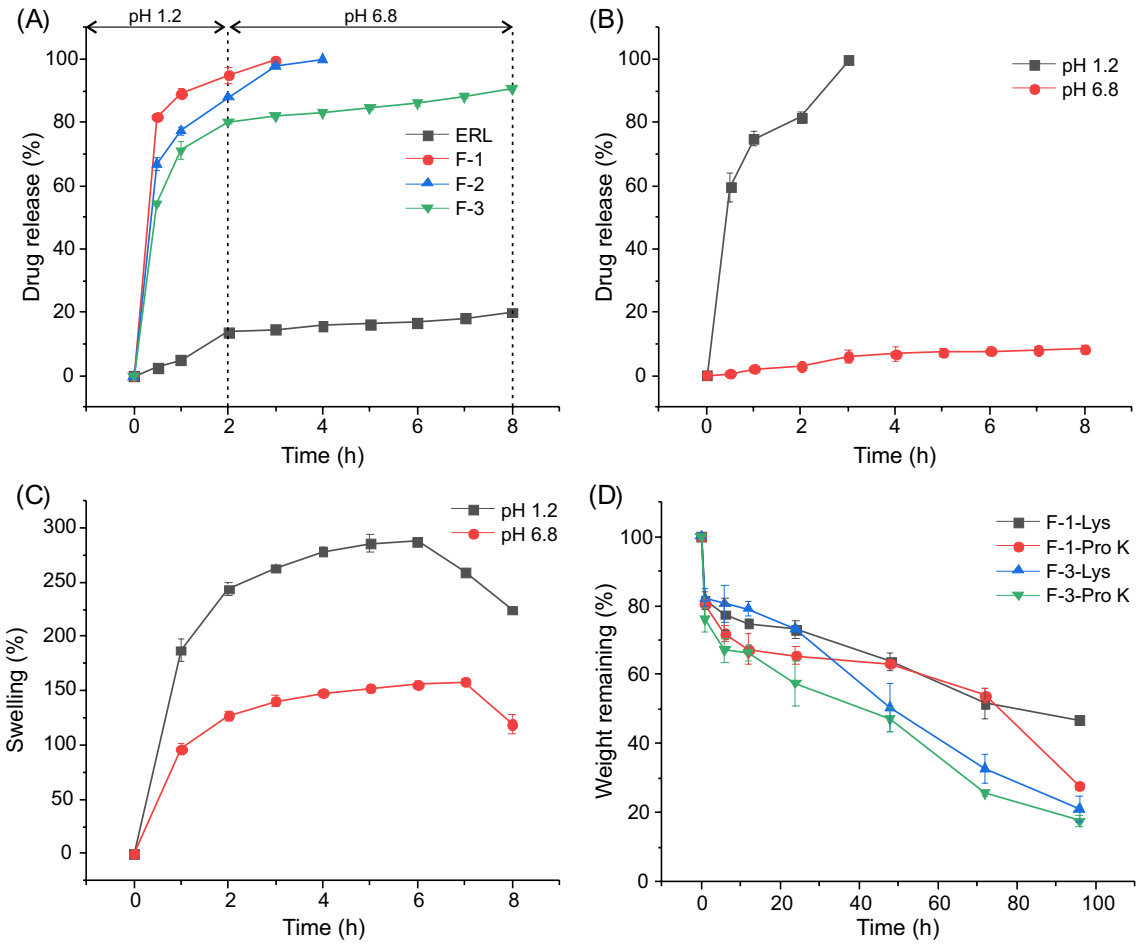

Fig. 4 Drug release patterns of ERL and various matrices (F-1, F-2 and F-3) (**A**). Drug release (**B**) and swelling (**C**) profiles of F-3 at acidic (pH 1.2) and neutral (phosphate buffer, pH 6.8) media. Biodegradation of F-1 and F-3 in the presence of proteinase K and lysozyme enzymes (**D**)

be attributed to the enhanced solubility of drug molecules into the polymeric matrices. The molecular dispersion of poorly soluble ERL into the polymeric matrices could increase its solubility [41–43]. The intercalated or exfoliated MMT within the NCs could also entrap drug molecules and eventually augment their solubility [11]. Among different formulations, the IPN beads containing highest clay contents (F-3) exhibited sustained ERL elution patterns as compared to other matrices (F-1 and F-2) (Fig. 4A). For instance, the F-1 and F-2 demonstrated 100% drug release within 4 h, while F-3 exhibited more delayed ERL elution patterns (~80% drug release within 8 h). The delayed drug release profile of F-3 was plausibly owing to a greater degree of tortuosity and decreased free volume spaces of the GA/zinc acetate crosslinked IPN beads, which could eventually restrain ERL diffusion through the biopolymeric matrices [34]. In addition, a greater clay content in the beads (F-3) could efficiently intercalate the drug molecules into the MMT plates, which might act as drug reservoirs and reduce the diffusion process for the entrapped cargo [44]. Interestingly, the MMT-reinforced matrices (F2 and F-3) conferred improved DE and MDT values as compared to clay-free beads (Table S1). The beads with highest MMT contents (F-3) were selected to assess their pH-dependent drug release profiles as these revealed a comparatively delayed drug release patterns with reference to other formulations (F-1 and F-2). The F-3 also revealed an exceptionally faster drug elution rate under an acidic environment relative to the neutral pH ($p < 0.05$) (Fig. 4B). This could be accredited to the enhanced solubility of ERL in acidic pH, increasing its diffusivity through the biopolymeric matrices into acidic medium. Additionally, the protonation of ERL's nitrogen atoms under acidic condition could disturb various non-covalent interactions (*i.e.,* hydrogen bonding and hydrophobic interactions) between the biopolymeric matrices and the entrapped drug molecules, leading to a faster drug release rate [21].

The drug release profiles of various IPN beads were fitted to different kinetic models to understand which one among them could be dominant in fitting the release data with a correlation coefficient closer to 1 (Fig. S4–S6 and Table S1). The ERL release patterns of different beads (F-1–F-3) mostly followed the Korsemeyer-Peppas kinetic model (correlation coefficient, $r^2 \sim 1$) with anomalous transport-driven drug release mechanisms (diffusion exponent, $n < 0.45$). The gel characteristic constants ($k_{KP)}$ of various IPN beads were variable (0.66–0.88), which indicated diverse structural and geometric features of matrices [23]. The late phase diffusion coefficient (D_L) values of different formulations were substantially higher than initial phase diffusion coefficient (D_I) values (Table S1). This could be ascribed to the weakening of matrix architecture following loosened or disintegrated biopolymeric chains [21].

Temperature and pH-Responsive Swelling

Various IPN beads conferred a reduction in their equilibrium % swelling in distilled water with an increase in temperature from 4 to 45 °C (Table S2). The hydrophilic characteristics of grafted PNIPA chains at 4 °C promoted higher swelling of beads. At elevated temperatures, the transition of grafted PNIPA chains from flexible coil structures to compact globular states could reduce the water absorption capacity of the beads [21]. Flory–Rehner equations were utilized to analyze equilibrium % swelling of beads at different temperatures and calculate their various structural parameters, including Flory–Huggins interaction parameter (χ), volume fraction in the swollen state (ϕ), molecular weight of the polymer chains between two neighboring crosslinks ($\overline{M}_c$) and the crosslinked density (ρ) (Table S2) [45]. Increasing the temperature of swelling media from 4 to 45 °C incessantly enhanced the $\overline{M}_c$ values of beads, while decreasing their crosslink density (ρ).

Among various matrices, the beads with highest MMT contents (F-3) were further selected to examine their pH-dependent swelling patterns based on their slower drug release profiles, which might be strongly influenced by their swelling behavior. As shown in Fig. 4C and Fig. S1, MMT-reinforced beads (F-3) presented a pH-sensitive swelling profile following their incubation in acidic (pH 1.2) and neutral (phosphate buffer, pH 6.8) media at 37 °C. In acidic pH, the swelling of beads was dramatically increased compared to that in a neutral environment ($p < 0.05$). This could be attributed to the expanded polymeric network in acidic pH resulting from the electrostatic repulsions among polymeric chains [46], eventually displaying a comparatively higher swelling rate and water penetration velocity (Table S3). The substantial swelling of beads after 6–7 h might destroy their integrity, resulting in partial disintegration of the matrices in the aqueous media and mass loss [47].

Biodegradation

The MMT-free (F-1) and MMT-reinforced beads (F-3) were exposed to lysozyme and proteinase k enzymes to assess the influence of MMT on their biodegradation. The enzymatic degradation resulted in progressive mass loss of both matrices with time (Fig. 4D). The proteinase k and lysozyme could penetrate into the beads and hydrolyze abundant amide and glycosidic linkages of the biopolymeric backbone, respectively, gradually losing matrix integrity [48]. As compared to the clay-free matrices (F-1), the MMT-containing beads (F-3) exhibited higher weight loss. Possibly, MMT could provide more surface area and catalytic reaction sites, allowing enzymes to more efficiently bind and break down the polymeric chains [49].

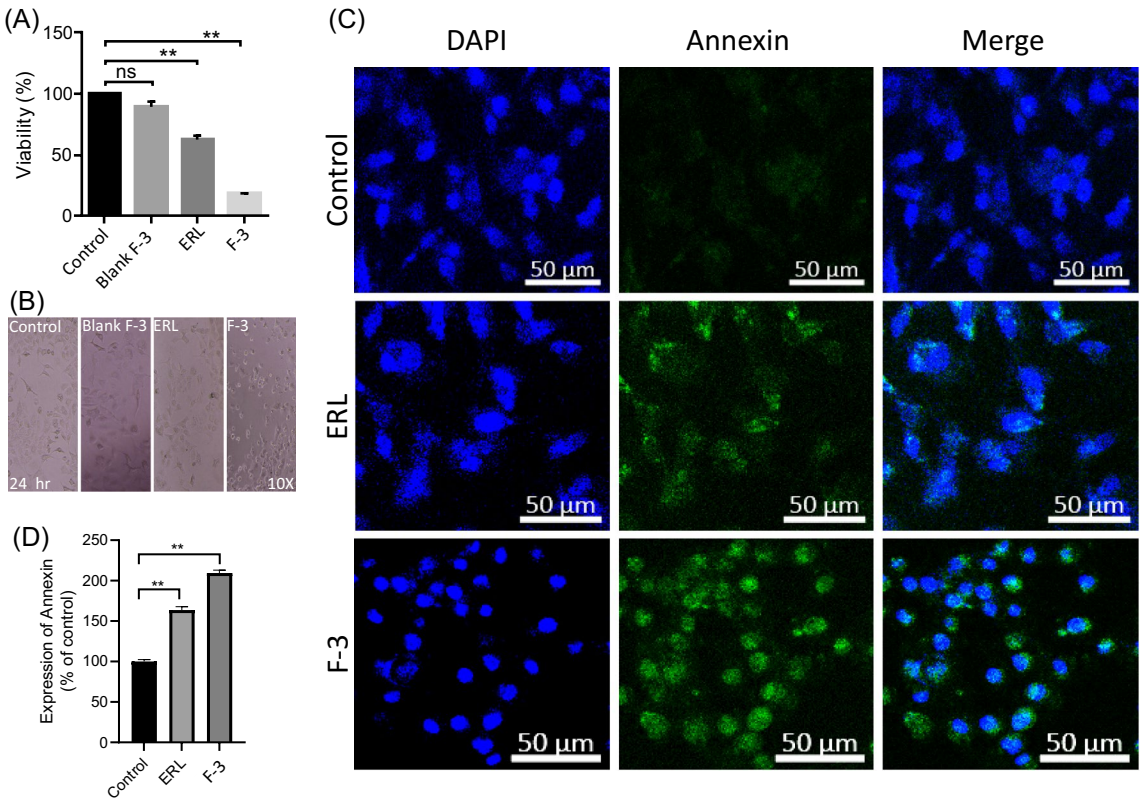

Fig. 5 Cell viability of blank control, blank F-3, pure ERL, and drug loaded F-3 (**A**) and cellular morphologies of MDA-MB-231 cells following treatment with blank control, blank F-3, pure ERL and drug loaded F-3 (**B**). The expression of Annexin-V on the MDA-MB-231 cells following treatment with blank control, pure ERL and drug loaded F-3 (**C** and **D**)

Cytotoxicity and Cellular Morphology

The viability of the MDA-MB-231 cells was assessed after 24 h of treatment with pure ERL, placebo F-3 and ERL-loaded formulation (F-3), which contained an equivalent ERL dose of 27.5 µM (*i.e.,* the IC_{50} value). The cells displayed substantially more sensitivity to the pure drug and the ERL-loaded formulation (F-3) compared to the vehicle control ($p < 0.05$) (Fig. 5A). F-3 more effectively suppressed cancer cell growth than pure ERL ($p < 0.05$), suggesting that the drug-loaded matrixes had a higher anti-proliferative effect [21]. Additionally, ERL-free matrices (viz., placebo F-3) did not elicit the cytotoxicity on MDA-MB-231 cells, demonstrating their non-toxic nature. The IPN beads could therefore be utilized as a safe drug delivery vehicle [50].

Before examining cytotoxicity of various samples by MTT assay protocol, the images of the cells treated with vehicle control, blank F-3, ERL and drug-loaded F-3 were captured to examine their morphological changes (Fig. 5B). The blank F-3 treated cells were live and exhibited well spread and flattened morphology with normal rate of proliferation, which was similar to that of vehicle control treated group. This indicated that the blank F-3 was biocompatible to the cells. On the other hand, following treatment with ERL and drug loaded formulation (F-3), the cells became smaller, rounded and non-adherent, which were the characteristics of the dead cells [19].

Apoptosis

The immunofluorescence studies were conducted to determine the impacts of pure ERL and the drug-loaded formulation (F-3) on the apoptosis of MDA-MB-231 cells. ERL-loaded formulation (F-3) amplified the production of Annexin-V, a cell apoptosis marker, in cells in comparison to pristine drug [28]. Following treatment with F-3, more nuclear fragmentation of MDA-MB-231 cells was observed relative to that of pure ERL. This was indicative of a stronger apoptosis-inducing potential of F-3 as compared to native ERL (Figs. 5C, D). It suggested that F-3 could more effectively deliver ERL to the tumor cells and trigger the cell death [51].

Conclusions

The findings of the current research endeavors clearly demonstrated the capabilities of the dual crosslinked CTX/LMP-based IPN beads to deliver ERL to the TNBC cells. The graft copolymerization protocol was exploited to afford three different CTX/MMT NCs with varying MMT concentrations (0, 10, and 20% w/w of NIPA). The concurrent ionotropic gelation and covalent crosslinking methods were then adopted to produce the ERL-entrapped CTX/LMP-based IPN beads. Among various IPN matrices, the beads with the highest MMT contents (F-3) demonstrated excellent drug loading (DEE, 86.73%), a delayed drug release profile (Q_{8h}, 80%), temperature and pH-responsive swelling patterns and acceptable biodegradability and biocompatibility. Additionally, as compared to pure ERL, the IPN beads (F-3) displayed superior anti-proliferative and apoptosis-inducing potentials on MDA-MB-231 cells. In general, the ERL-loaded IPN beads could be facilely fabricated without requiring any complicated steps and might serve as an emerging treatment option for TNBC therapy. However, the structural characterization of the biodegraded products of developed beads and evaluation of their stability warrant further investigations.

Supplementary Information The online version contains supplementary material available at https://doi.org/10.1007/s10924-023-03127-y.

Author Contributions YFA: Preparation and characterization of drug-loaded formulations, writing, reviewing and editing; HB: Conceptualization, characterization of drug-loaded formulations, supervision, writing, reviewing and editing; AT: Cell culture experiments of various scaffolds; YFA and HB contributed equally.

Funding The present work was supported by the fellowship of China Postdoctoral Science Foundation (Grant no. 2021MD703857; grant recipient, Dr. Hriday Bera).

Declarations

Conflict of interest The authors have no conflict of interest to disclose.

References

1. Li L, Yang WW, Xu DG (2019) Stimuli-responsive nanoscale drug delivery systems for cancer therapy. J Drug Target 27(4):423–433. https://doi.org/10.1080/1061186X.2018.1519029
2. Senapati S, Mahanta AK, Kumar S, Maiti P (2018) Controlled drug delivery vehicles for cancer treatment and their performance. Signal Transduct Target Ther 3(1):7. https://doi.org/10.1038/s41392-017-0004-3
3. Salari N, Faraji F, Torghabeh FM, Faraji F, Mansouri K, Abam F et al (2022) Polymer-based drug delivery systems for anticancer drugs: a systematic review. Cancer Treat Res Commun 32:100605. https://doi.org/10.1016/j.ctarc.2022.100605
4. Nagaraja K, Rao KM, Rao KSVK, Han SS (2022) Dual responsive tamarind gum-co-poly(N-isopropyl acrylamide-co-ethylene glycol vinyl ether) hydrogel: a promising device for colon specific anticancer drug delivery. Colloids Surf A 641:128456. https://doi.org/10.1016/j.colsurfa.2022.128456
5. Gupta NR, Torris ATA, Wadgaonkar PP, Rajamohanan PR, Ducouret G, Hourdet D et al (2015) Synthesis and characterization of PEPO grafted carboxymethyl guar and carboxymethyl tamarind as new thermo-associating polymers. Carbohyd Polym 117:331–338. https://doi.org/10.1016/j.carbpol.2014.09.073
6. Dey S, Chandra Nandy B, De Narayan J, Hasnain MS, Nayak AK (2019) Chapter 12 - Tamarind gum in drug delivery applications. In: Hasnain MS, Nayak AK (eds) Natural polysaccharides in drug delivery and biomedical applications. Academic Press, Cambridge, pp 285–306
7. Jana S, Sharma R, Maiti S, Sen KK (2016) Interpenetrating hydrogels of O-carboxymethyl Tamarind gum and alginate for monitoring delivery of acyclovir. Int J Biol Macromol 92:1034–1039. https://doi.org/10.1016/j.ijbiomac.2016.08.017
8. Dhand AP, Galarraga JH, Burdick JA (2021) Enhancing biopolymer hydrogel functionality through interpenetrating networks. Trends Biotechnol 39(5):519–538. https://doi.org/10.1016/j.tibtech.2020.08.007
9. Ren J, Li J, Xu Z, Du Z, Cheng F (2021) Feasibility of thermo-sensitive P(NIPAM-MBA) hydrogels as novel stripping agents for osmotic membrane distillation. J Environ Chem Eng 9(4):105370. https://doi.org/10.1016/j.jece.2021.105370
10. Khodami S, Kaniewska K, Karbarz M, Stojek Z (2023) Antioxidant ability and increased mechanical stability of hydrogel nanocomposites based on N-isopropylacrylamide crosslinked with Laponite and modified with polydopamine. Eur Polymer J 187:111876. https://doi.org/10.1016/j.eurpolymj.2023.111876
11. Park JH, Shin HJ, Kim MH, Kim JS, Kang N, Lee JY et al (2016) Application of montmorillonite in bentonite as a pharmaceutical excipient in drug delivery systems. J Pharm Investig 46(4):363–375. https://doi.org/10.1007/s40005-016-0258-8
12. Bodnár K, Hudson SP, Rasmuson ÅC (2020) Drug loading and dissolution properties of dalcetrapib-montmorillonite nanocomposite microparticles. Org Process Res Dev 24(6):977–987. https://doi.org/10.1021/acs.oprd.9b00460
13. Doniparthi J, B JJ. (2020) Novel tamarind seed gum-alginate based multi-particulates for sustained release of dalfampridine using response surface methodology. Int J Biol Macromol 144:725–41. https://doi.org/10.1016/j.ijbiomac.2019.11.203
14. Jana S, Pramanik R, Nayak AK, Sen KK (2022) Gellan gum (GG)-based IPN microbeads for sustained drug release. J Drug Deliv Sci Technol 69:103034. https://doi.org/10.1016/j.jddst.2021.103034
15. Kulkarni RV, Mutalik S, Mangond BS, Nayak UY (2011) Novel interpenetrated polymer network microbeads of natural polysaccharides for modified release of water soluble drug: in-vitro and in-vivo evaluation. J Pharm Pharmacol 64(4):530–540. https://doi.org/10.1111/j.2042-7158.2011.01433.x
16. Li DQ, Li J, Dong HL, Li X, Zhang JQ, Ramaswamy S, Xu F (2021) Pectin in biomedical and drug delivery applications: a review. Int J Biol Macromol 185:49–65. https://doi.org/10.1016/j.ijbiomac.2021.06.088
17. Abdelgalil AA, Al-Kahtani HM, Al-Jenoobi FI (2020) Chapter Four - Erlotinib. In: Brittain HG (ed) Profiles of drug substances excipients and related methodology. Academic Press, Cambridge, pp 93–117
18. Liu Y, Ma X, Zhu Y, Lv X, Wang P, Feng L (2022) pH-responsive nanomedicine co-encapsulated with Erlotinib and chlorin e6 can enable effective treatment of triple negative breast cancer via reprogramming tumor vasculature. Chem Eng J 437:135305. https://doi.org/10.1016/j.cej.2022.135305
19. Bera H, Abbasi YF, Lee Ping L, Marbaniang D, Mazumder B, Kumar P et al (2020) Erlotinib-loaded carboxymethyl temarind

gum semi-interpenetrating nanocomposites. Carbohyd Poly 230:115664. https://doi.org/10.1016/j.carbpol.2019.115664
20. Ghorbani M, Nezhad-Mokhtari P, Mahmoodzadeh F (2021) Incorporation of oxidized pectin to reinforce collagen/konjac glucomannan hydrogels designed for tissue engineering applications. Macromol Res 29(4):289–296. https://doi.org/10.1007/s13233-021-9033-4
21. Bera H, Abbasi YF, Gajbhiye V, Ping LL, Salve R, Kumar P et al (2021) Chemosensitivity assessments of curdlan-doped smart nanocomposites containing erlotinib HCl. Int J Biol Macromol 181:169–179. https://doi.org/10.1016/j.ijbiomac.2021.03.152
22. Mathematical models of drug release (2015). In: Bruschi ML (ed) Strategies to modify the drug release from pharmaceutical systems. Woodhead Publishing, Cambridge, pp 63–86
23. Bera H, Abbasi YF, Yoke FF, Seng PM, Kakoti BB, Ahmmed SKM, Bhatnagar P (2019) Ziprasidone-loaded arabic gum modified montmorillonite-tailor-made pectin based gastroretentive composites. Int J Biol Macromol 129:552–563. https://doi.org/10.1016/j.ijbiomac.2019.01.171
24. Erfani A, Flynn NH, Aichele CP, Ramsey JD (2020) Encapsulation and delivery of protein from within poly(sulfobetaine) hydrogel beads. J Appl Polym Sci 137(40):49550. https://doi.org/10.1002/app.49550
25. Kulkarni AR, Soppimath KS, Aminabhavi TM, Dave AM, Mehta MH (2000) Glutaraldehyde crosslinked sodium alginate beads containing liquid pesticide for soil application. J Control Release 63(1):97–105. https://doi.org/10.1016/S0168-3659(99)00176-5
26. Kevadiya BD, Rajkumar S, Bajaj HC, Chettiar SS, Gosai K, Brahmbhatt H et al (2014) Biodegradable gelatin–ciprofloxacin–montmorillonite composite hydrogels for controlled drug release and wound dressing application. Colloids Surf, B 122:175–183. https://doi.org/10.1016/j.colsurfb.2014.06.051
27. Gerlier D, Thomasset N (1986) Use of MTT colorimetric assay to measure cell activation. J Immunol Methods 94(1):57–63. https://doi.org/10.1016/0022-1759(86)90215-2
28. Krey JF, Drummond M, Foster S, Porsov E, Vijayakumar S, Choi D et al (2016) Annexin A5 is the most abundant membrane-associated protein in stereocilia but is dispensable for hair-bundle development and function. Sci Rep 6(1):27221. https://doi.org/10.1038/srep27221
29. Chakka VP, Zhou T (2020) Carboxymethylation of polysaccharides: synthesis and bioactivities. Int J Biol Macromol 165:2425–2431. https://doi.org/10.1016/j.ijbiomac.2020.10.178
30. Kulkarni RV, Sa B (2008) Enteric delivery of ketoprofen through functionally modified poly(acrylamide-grafted-xanthan)-based pH-sensitive hydrogel beads: preparation, in vitro and in vivo evaluation. J Drug Target 16(2):167–177. https://doi.org/10.1080/10611860701792399
31. Ma J, Zhang L, Fan B, Xu Y, Liang B (2008) A novel sodium carboxymethylcellulose/poly (N-isopropylacrylamide)/Clay semi-IPN nanocomposite hydrogel with improved response rate and mechanical properties. J Polym Sci, Part B: Polym Phys 46(15):1546–1555. https://doi.org/10.1002/polb.21490
32. Das S, Ng KY, Ho PC (2010) Formulation and optimization of zinc-pectinate beads for the controlled delivery of resveratrol. AAPS PharmSciTech 11(2):729–742. https://doi.org/10.1208/s12249-010-9435-7
33. Rudra R, Kumar V, Kundu pp. (2015) Acid catalysed cross-linking of poly vinyl alcohol (PVA) by glutaraldehyde: effect of crosslink density on the characteristics of PVA membranes used in single chambered microbial fuel cells. RSC Adv 5(101):83436–83447. https://doi.org/10.1039/C5RA16068E
34. Bulut E (2021) Development and optimization of Fe^{3+}-crosslinked sodium alginate-methylcellulose semi-interpenetrating polymer network beads for controlled release of ibuprofen. Int J Biol Macromol 168:823–833. https://doi.org/10.1016/j.ijbiomac.2020.11.147
35. Li H, Qiu H, Wang J, Sun Z (2020) Erlotinib–silk fibroin nanoparticles in inhibiting tumor. Polym Bull 77(8):4325–4334. https://doi.org/10.1007/s00289-019-02946-1
36. Pongjanyakul T, Rongthong T (2010) Enhanced entrapment efficiency and modulated drug release of alginate beads loaded with drug–clay intercalated complexes as microreservoirs. Carbohyd Polym 81(2):409–419. https://doi.org/10.1016/j.carbpol.2010.02.038
37. Gomes RF, Lima LRM, Feitosa JPA, Paula HCB, de Paula RCM (2020) Influence of galactomannan molar mass on particle size galactomannan-grafted-poly-N-isopropylacrylamide copolymers. Int J Biol Macromol 156:446–453. https://doi.org/10.1016/j.ijbiomac.2020.04.004
38. Jahanizadeh S, Yazdian F, Marjani A, Omidi M, Rashedi H (2017) Curcumin-loaded chitosan/carboxymethyl starch/montmorillonite bio-nanocomposite for reduction of dental bacterial biofilm formation. Int J Biol Macromol 105(Pt 1):757–763. https://doi.org/10.1016/j.ijbiomac.2017.07.101
39. Rampaka R, Ommi K, Chella N (2021) Role of solid lipid nanoparticles as drug delivery vehicles on the pharmacokinetic variability of Erlotinib HCl. J Drug Deliv Sci Technol 66:102886. https://doi.org/10.1016/j.jddst.2021.102886
40. Gontijo SML, Guimarães PPG, Viana CTR, Denadai ÂML, Gomes ADM, Campos PP et al (2015) Erlotinib/hydroxypropyl-β-cyclodextrin inclusion complex: characterization and in vitro and in vivo evaluation. J Incl Phenom Macrocycl Chem 83(3):267–279. https://doi.org/10.1007/s10847-015-0562-3
41. Choi MJ, Woo MR, Choi HG, Jin SG (2022) Effects of polymers on the drug solubility and dissolution enhancement of poorly water-soluble rivaroxaban. Int J Mol Sci. https://doi.org/10.3390/ijms23169491
42. Mazumder S, Dewangan AK, Pavurala N (2017) Enhanced dissolution of poorly soluble antiviral drugs from nanoparticles of cellulose acetate based solid dispersion matrices. Asian J Pharm Sci 12(6):532–541. https://doi.org/10.1016/j.ajps.2017.07.002
43. Lang W, Tagami T, Kang HJ, Okuyama M, Sakairi N, Kimura A (2023) Partial depolymerization of tamarind seed xyloglucan and its functionality toward enhancing the solubility of curcumin. Carbohydr Polym 307:120629. https://doi.org/10.1016/j.carbpol.2023.120629
44. Yadav H, Agrawal R, Panday A, Patel J, Maiti S (2022) Polysaccharide-silicate composite hydrogels: Review on synthesis and drug delivery credentials. J Drug Deliv Sci Technol 74:103573. https://doi.org/10.1016/j.jddst.2022.103573
45. Singh B, Sharma V, Chauhan D (2010) Gastroretentive floating sterculia–alginate beads for use in antiulcer drug delivery. Chem Eng Res Des 88(8):997–1012. https://doi.org/10.1016/j.cherd.2010.01.017
46. Mahdavinia G, Afzali A, Etemadi H, Hosseinzadeh H (2017) Magnetic/pH-sensitive nanocomposite hydrogel based carboxymethyl cellulose-g-polyacrylamide/montmorillonite for colon targeted drug deliver. Nanomed Res J 2(2):111–122. https://doi.org/10.22034/NMRJ.2017.58964.1058
47. Bajpai SK, Kirar N (2016) Swelling and drug release behavior of calcium alginate/poly (sodium acrylate) hydrogel beads. Des Monomers Polym 19(1):89–98. https://doi.org/10.1080/15685551.2015.1092016
48. Wang D, Lv R, Ma X, Zou M, Wang W, Yan L et al (2018) Lysozyme immobilization on the calcium alginate film under sonication: development of an antimicrobial film. Food Hydrocolloids 83:1–8. https://doi.org/10.1016/j.foodhyd.2018.04.021
49. Peng K, Fu L, Yang H, Ouyang J (2016) Perovskite $LaFeO_3$/montmorillonite nanocomposites: synthesis, interface characteristics

and enhanced photocatalytic activity. Sci Rep 6(1):19723. https://doi.org/10.1038/srep19723
50. Upadhyay M, Adena SKR, Vardhan H, Yadav SK, Mishra B (2019) Locust bean gum and sodium alginate based interpenetrating polymeric network microbeads encapsulating capecitabine: improved pharmacokinetics, cytotoxicity & in vivo antitumor activity. Mater Sci Eng C 104:109958. https://doi.org/10.1016/j.msec.2019.109958
51. Vaidya B, Parvathaneni V, Kulkarni NS, Shukla SK, Damon JK, Sarode A et al (2019) Cyclodextrin modified erlotinib loaded PLGA nanoparticles for improved therapeutic efficacy against non-small cell lung cancer. Int J Biol Macromol 122:338–347. https://doi.org/10.1016/j.ijbiomac.2018.10.181

Publisher's Note Springer Nature remains neutral with regard to jurisdictional claims in published maps and institutional affiliations.

Springer Nature or its licensor (e.g. a society or other partner) holds exclusive rights to this article under a publishing agreement with the author(s) or other rightsholder(s); author self-archiving of the accepted manuscript version of this article is solely governed by the terms of such publishing agreement and applicable law.